https://doi.org/10.1007/s41230-025-5100-3

Development of a cost-effective Fe-P-C nanocrystalline alloy with high magnetic induction and ductility via annealing-free melt-spinning

Jing Ding[1], *Cong Liu[2], Zhao-can Li[1], Wen-chao Liu[1], Xiao-long Wang[1], Ji-li Tian[1], Shu-qiang Lü[1], and **Sheng-li Zhu[3, 4]

1. School of Energy and Machinery, Dezhou University, Dezhou 253023, Shandong, China

2. School of Materials Science and Engineering, Hebei University of Technology, Tianjin 300130, China

3. School of Materials Science and Engineering, Tianjin University, Tianjin 300072, China

4. School of Materials Science and Engineering, Lanzhou Jiaotong University, Lanzhou 730070, China

Abstract: A cost-effective Fe-P-C nanocrystalline alloy ($Fe_{85}P_9C_6$) was developed via melt-spinning by eliminating expensive alloying elements and post-annealing steps. The microstructure consists of an amorphous matrix with uniformly dispersed nanocrystalline clusters, featuring an average size of approximately 5 nm. This dual-phase structure remains thermally stable up to 569 K and results in excellent magnetic and mechanical performance, including a high saturation magnetic induction of 1.69 T, Vickers hardness of 621 HV, and outstanding bending ductility. Crystallization proceeds via the transformation of a metastable fcc-(Fe, P, C) phase into α-Fe, Fe_3C, and Fe_3P, driven by internal stress arising from atomic size mismatch. Continuous heating and cooling transformation diagrams further reveal that this process can be precisely controlled to optimize phase evolution. The high Fe content and stress-relaxed nanocrystalline clusters contribute to enhanced in-plane magnetic anisotropy and rapid domain response. This simplified, annealing-free approach not only reduces material and processing costs but also provides a viable pathway for scalable fabrication of next-generation soft magnetic alloys with superior performance and manufacturability.

Keywords: amorphous; nanocrystalline; saturation magnetic induction; ductility

CLC numbers: TG143 **Document code:** A **Article ID:** 1672-6421(2026)02-169-10

1 Introduction

The growing demand for energy-efficient electrical equipment, such as motors, generators, and transformers, has driven the development of soft magnetic materials with superior performance. Fe-based amorphous and nanocrystalline (AN) alloys are promising candidates due to their excellent magnetic properties and favorable processability. Conventionally, commercial soft magnetic nanocrystalline alloy ribbons are produced via a two-step process: melt-spinning to form a single-phase amorphous precursor, followed by annealing to induce nanocrystallization. Despite its effectiveness, this approach requires costly equipment, precise thermal control, and multiple processing stages, all of which contribute to increased manufacturing costs as well as the risk of oxidation and embrittlement.

To overcome these limitations, recent efforts have focused on developing annealing-free materials with high magnetic performance. Over the past three decades, significant advances have been made in nanocrystalline alloy systems such as Finemet, NanoPerm, and HitPerm, based on FeSiBNbCu, FeZrB(Cu), and FeCoZrBCu compositions, respectively[1, 2]. Despite their favorable soft magnetic properties, these alloys often incorporate expensive and oxidation-sensitive elements (e.g., Zr), along with substantial amounts of non-magnetic constituents (e.g., Cu)[3-6]. These additions improve thermal stability and glass-forming ability but simultaneously reduce magnetic induction and increase costs. The maximum saturation magnetic induction (B_s) of most commercial AN alloys,

***Cong Liu**

Postdoctoral researcher. Her research interest primarily focuses on the design and properties of amorphous alloys.

E-mail: liucong010243@163.com

****Sheng-li Zhu**

E-mail: slzhu@tju.edu.cn

Received: 2025-05-03; Revised: 2025-05-27; Accepted: 2025-07-24

such as METGLAS2605, remains around 1.63 T, limited by the relatively low content of magnetic elements[7, 8]. A promising strategy to enhance B_s and reduce cost involves increasing the fraction of magnetic elements while eliminating expensive alloying additions. In addition, optimizing the melt-spinning process to promote high-density quenched cluster formation may enable direct development of composite structures, eliminating the need for post-spinning annealing and simplifying fabrication[9, 10].

Among Fe-based alloy systems, Fe-P-C alloys show significant potential. First reported by Duwez et al.[10] in 1967, alloys containing approximately 6wt.% P and 1.7wt.% C were among the earliest to exhibit notable magnetic properties in the amorphous state. Subsequent developments, such as $Fe_{80}P_{11}C_9$ (with a B_s of 1.37 T, increasing to 1.49 T after annealing) and $Fe_{80}P_{13}C_7$ (B_s=1.53 T), underscored the sensitivity of magnetic performance to subtle compositional variations[11, 12]. However, Fe-P-C alloys with Fe contents exceeding 81at.% receive relatively little attention. The effects of such high Fe concentrations on magnetic properties, structural evolution, and thermal stability remain inadequately understood. Conventional Fe-P-C alloys typically contain more than 11at.% P to enhance glass-forming ability, which unfortunately also increases brittleness and the risk of fracture during processing. Reducing the P content may offer a promising strategy to retain desirable soft magnetic properties while improving mechanical toughness and manufacturability.

This study focuses on the development of an Fe-P-C alloy system with Fe content above 81at.% and P content below 11at.%. The formation mechanism, microstructure, thermal behavior, mechanical properties, and soft magnetic characteristics were systematically investigated to evaluate its potential as a high-performance, annealing-free soft magnetic material.

2 Experimental methods

Ternary alloy ingots with nominal compositions of $Fe_{82}P_{11.7}C_{6.3}$, $Fe_{84}P_{10.7}C_{5.3}$, and $Fe_{85}P_9C_6$ (in atomic percentage) were successfully prepared by induction melting high-purity Fe (99.9wt.%), Fe_3P fragments (99.5wt.%), and C fragments (99.9wt.%) in an argon atmosphere. The alloy ingots were processed into melt-spun ribbons. For the $Fe_{82}P_{11.7}C_{6.3}$ and $Fe_{84}P_{10.7}C_{5.3}$ alloys, ribbons with a thickness of approximately 25 μm and a width of ~1.2 mm were obtained, and all subsequent characterizations and property evaluations were based on these ribbons. In contrast, for the $Fe_{85}P_9C_6$ alloy, ribbons with thicknesses of 23, 24, 25, and 26 μm were fabricated to further examine the effect of ribbon thickness on structure and properties. For consistency, all cross-comparisons among the three compositions in this work were conducted on ribbons with fixed thicknesses: $Fe_{82}P_{11.7}C_{6.3}$ (25 μm), $Fe_{84}P_{10.7}C_{5.3}$ (25 μm), and $Fe_{85}P_9C_6$ (23 μm). The alloy ingots were further processed into ribbons with thicknesses ranging from 23 μm to 26 μm and width of approximately 1.2 mm using the single roller melt spinning technique. Microstructural characterization was conducted using optical microscopy (OM), X-ray diffraction (XRD), transmission electron microscopy (TEM), and high-resolution transmission electron microscopy (HRTEM) to analyze the phase constitution and structural features of the alloys. The thermal stability of the as-quenched ribbons was evaluated utilizing differential scanning calorimetry (DSC) at a constant heating rate of 0.67 $K \cdot s^{-1}$ under a continuous flow of high-purity argon gas. Magnetic properties were evaluated using a vibrating sample magnetometer (VSM). Coercivity (H_c) was measured using a DC *B-H* loop analyzer under a maximum applied field of 800 $A \cdot m^{-1}$, with ribbon samples approximately 7 cm in length. Magnetic domain structures were observed using a magneto-optical Kerr effect (MOKE) microscope (Imager D2m) on the air-side surface of the as-spun ribbons. To investigate domain evolution under low-field cyclic magnetization, an external magnetic field sweeping from −1 to +1 $kA \cdot m^{-1}$ was applied. Particular attention was paid to the domain morphology changes within the 0 to 1 $kA \cdot m^{-1}$ field range, aiming to elucidate the magnetization dynamics and domain response mechanisms in the amorphous/nanocrystalline state. Mechanical performance was assessed through Vickers hardness testing under a 0.98 N load. Bending ductility was qualitatively evaluated via 180° manual bending tests, ribbons that withstood complete bending without visible fracture were considered to exhibit excellent flexibility.

3 Results

Figure 1(a) shows the XRD patterns of $Fe_{82}P_{11.7}C_{6.3}$, $Fe_{84}P_{10.7}C_{5.3}$, and $Fe_{85}P_9C_6$ alloy ribbons in the melt-spun state. It can be clearly seen that both the $Fe_{82}P_{11.7}C_{6.3}$ and $Fe_{84}P_{10.7}C_{5.3}$ samples exhibit the halo peaks characteristic of amorphous materials, indicating their amorphous structure. Although both alloys display amorphous features in the XRD patterns, TEM analysis for the $Fe_{84}P_{10.7}C_{5.3}$ alloy was further performed because its higher Fe content may reduce the glass-forming ability, and thus requires additional confirmation. To confirm the absence of any crystalline phases in the $Fe_{84}P_{10.7}C_{5.3}$ alloy ribbon, Figs. 1(b), (c), and (d) present a bright-field TEM image, a selected-area electron diffraction (SAED) pattern, and a HRTEM image, respectively. Examination of the bright-field TEM images reveals no contrast variations suggestive of crystalline phases, while the SAED pattern confirms the fully amorphous nature of the structure. The HRTEM image further displays a uniform grayscale distribution, with no discernible grain boundaries or crystalline features. These findings demonstrate the formation of an amorphous phase in the melt-spun $Fe_{84}P_{10.7}C_{5.3}$ alloy ribbon. In comparison, the XRD pattern of the $Fe_{85}P_9C_6$ alloy ribbon exhibits tiny and sharp crystalline diffraction peaks superimposed on a broad scattering peak, indicating the precipitation of a small amount of crystalline phases within the amorphous matrix. Similar results were also reported by Murugaiyan et al[13, 14]. When the Fe content was increased to

83at.%–85at.%, crystallization peaks appeared in XRD patterns of melt-spun Fe-Si-B ribbons. Figure 1(e) presents the DSC curves for all the Fe-P-C melt-spun alloy ribbons in this study. The DSC curves of different composition alloys all exhibit two distinct exothermic peaks, indicating that the samples undergo crystallization reactions in two stages during the crystallization process. It can be observed that with the increase of Fe content, the crystallization temperature (T_x) gradually decreases from 675 K to 569 K (the specific T_x values can be found in Table 1), suggesting that the increase in Fe content facilitates the crystallization process. The T_x of amorphous alloys is predominantly influenced by the atomic bonding strength between their constituent elements[15, 16]. This bonding strength is essential for determining the alloy's thermal stability and crystallization behavior. Consequently, a reduction in the content of metalloid elements such as P and C in Fe-based amorphous alloys leads to a decrease in overall atomic bonding strength. This weakening of atomic interactions not only lowers the material's thermal stability but also reduces T_x.

Figures 2(a) to (c) show the OM images of the air-side free surfaces of the melt-spun $Fe_{82}P_{11.7}C_{6.3}$, $Fe_{84}P_{10.7}C_{5.3}$, and $Fe_{85}P_9C_6$ ribbons, respectively. The surfaces of the $Fe_{82}P_{11.7}C_{6.3}$ and $Fe_{84}P_{10.7}C_{5.3}$ ribbons appear relatively smooth, with no obvious morphological undulations, which is consistent with the amorphous nature of these samples as confirmed by XRD in Fig. 1(a). In contrast, the $Fe_{85}P_9C_6$ ribbon exhibits small protrusions and striped surface features, indicating a reduction in surface smoothness. These surface irregularities may be associated with the partial formation of nanocrystalline phases[17]. During rapid solidification, localized crystallization can lead to the release of latent heat, volume strain, and interfacial disturbances, which disrupt the equilibrium of surface tension in the melt and result in surface roughness after solidification. Figures 2(d) and (e) present the Vickers hardness (HV) and bending deformation behavior of the Fe-P-C alloy ribbons, with hardness values ranging from 621 HV to 724 HV, as summarized in Table 1. The results indicate a general trend of decreasing hardness with increasing Fe content, which is consistent with previous literature[18, 19]. This phenomenon is primarily attributed to changes in atomic bonding strength and the packing density of the amorphous structure[20, 21]. Specifically, an increased Fe content dilutes the concentration of non-metallic elements such as P and C, thereby reducing the number of strong covalent bonds within the alloy.

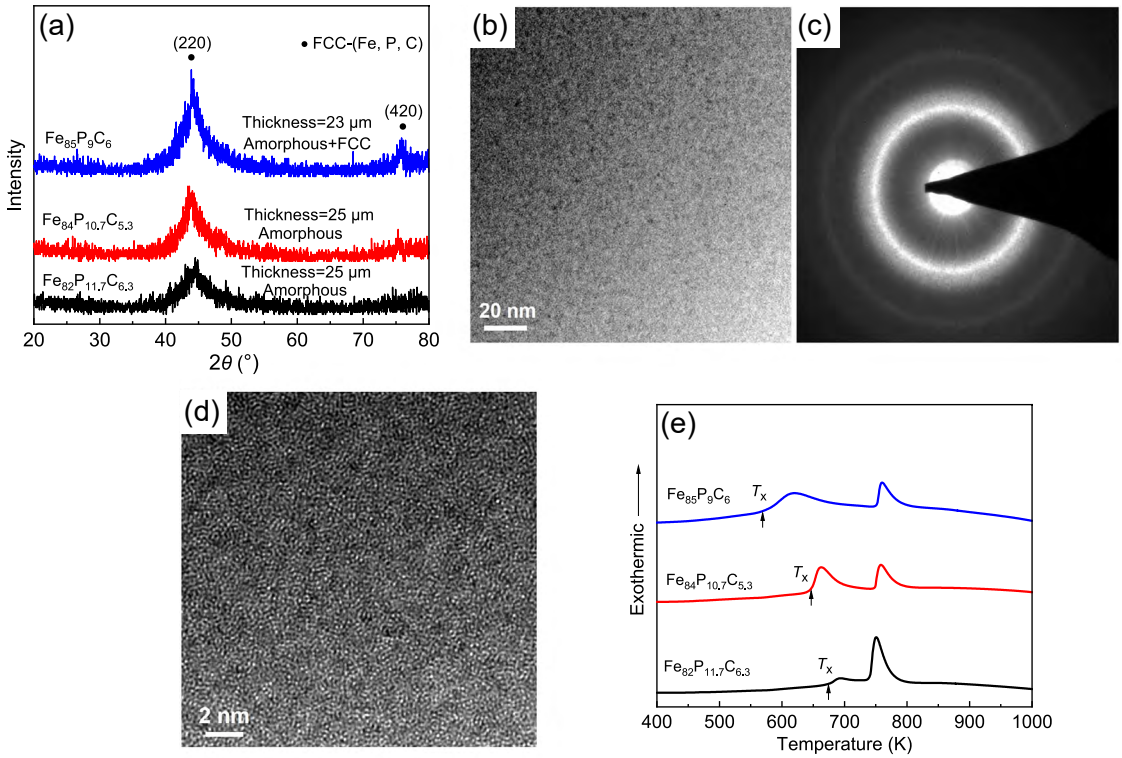

Fig. 1: XRD patterns (a), bright-field TEM image (b), SAED pattern (c), high-resolution TEM image of $Fe_{84}P_{10.7}C_{5.3}$ melt-spun alloy ribbon (d), and DSC curves of melt-spun $Fe_{82}P_{11.7}C_{6.3}$, $Fe_{84}P_{10.7}C_{5.3}$, and $Fe_{85}P_9C_6$ alloy ribbons (e)

Table 1: Summary of structure, thermal, mechanical and magnetic properties for melt-spun Fe-P-C alloy ribbons

Composition	Structure	T_x (K)	Hardness ($HV_{0.1}$)	B_s (T)	H_c (A·m^{-1})	Ductility
$Fe_{82}P_{11.7}C_{6.3}$	Amorphous	675	724	1.58	4.1	Ductile
$Fe_{84}P_{10.7}C_{5.3}$	Amorphous	649	670	1.60	7.2	Ductile
$Fe_{85}P_9C_6$	Amorphous+cluster	569	621	1.69	26.2	Ductile

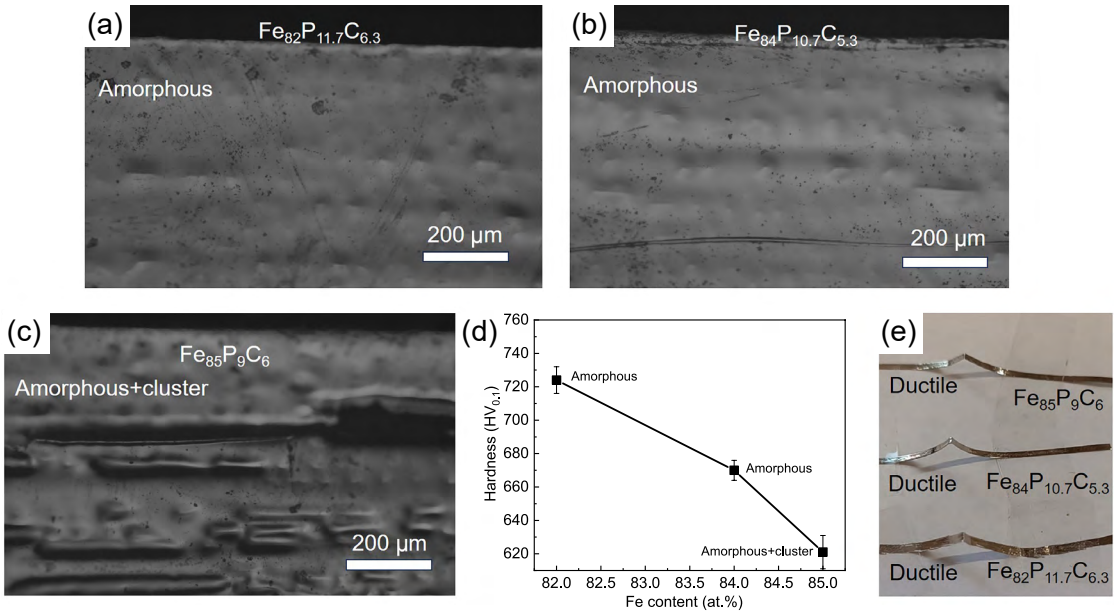

Fig. 2: OM images of air-side free surfaces of melt-spun $Fe_{82}P_{11.7}C_{6.3}$, $Fe_{84}P_{10.7}C_{5.3}$, and $Fe_{85}P_9C_6$ alloy ribbons (a–c), Vickers hardness of the corresponding samples (d), and ductile bending morphology of ribbons after bending tests (e)

This reduction weakens local atomic binding forces, leading to a decrease in overall hardness[20]. Furthermore, the elevated Fe content may decrease the atomic packing efficiency in the amorphous structure, resulting in a more loosely packed atomic network, which further diminishes the material's resistance to deformation[21]. Among the samples, the $Fe_{85}P_9C_6$ ribbon exhibits the lowest hardness of 621 HV, yet this value remains higher than that of many commercial Fe-Si soft magnetic materials (e.g., Fe-Si steel used in transformer cores, with a typical hardness of approximately 450 HV)[22]. Moreover, $Fe_{82}P_{11.7}C_{6.3}$, $Fe_{84}P_{10.7}C_{5.3}$, and $Fe_{85}P_9C_6$ melt-spun alloy ribbons are capable of being bent to 180° without visible cracking [Fig. 2(e)], suggesting that these alloys maintain a reasonable balance between high hardness and good bending ductility.

Since the XRD pattern in Fig. 1(a) of the 23 μm thick $Fe_{85}P_9C_6$ ribbon exhibits a small amount of crystalline phase, additional samples with thicknesses of 24 μm, 25 μm, and 26 μm were fabricated to further investigate the structural evolution with increasing thickness. As the ribbon thickness increases, the XRD patterns reveal enhanced intensities of crystalline peaks, indicating a gradual evolution of the crystalline phase, as shown in Fig. 3. Notably, although the content of fcc-(Fe, P, C) crystalline phase increases with ribbon thickness, the ductility of all samples was consistently confirmed by identical bending tests. This retention of ductility suggests that within the thickness range of 23 μm to 26 μm, the $Fe_{85}P_9C_6$ as-spun ribbons maintain a stable phase structure while delivering excellent bending performance. Such robustness across different dimensions highlights their structural stability and mechanical reliability, which are highly beneficial for subsequent processing, forming, and practical applications.

Figure 4(a) displays the *B-H* hysteresis loops of melt-spun $Fe_{82}P_{11.7}C_{6.3}$, $Fe_{84}P_{10.7}C_{5.3}$, and $Fe_{85}P_9C_6$ alloy ribbons, while Fig. 4(b) illustrates the variation of B_s with Fe content. As the Fe content increases from 82at.% to 85at.%, B_s correspondingly

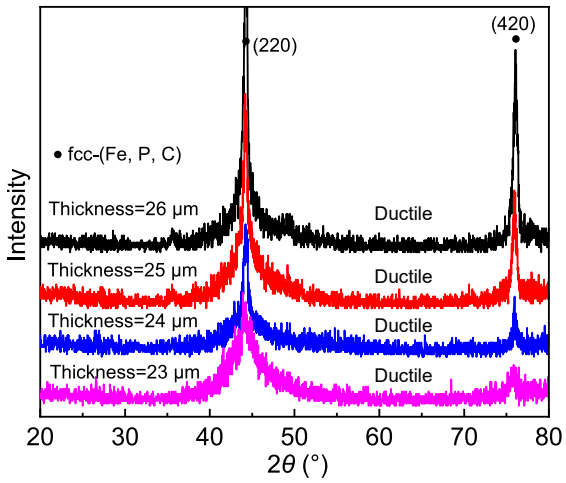

Fig. 3: XRD patterns and bending ductility of melt-spun $Fe_{85}P_9C_6$ alloy ribbons with different thicknesses

rises from 1.58 T to 1.69 T. This trend highlights the pivotal role of Fe concentration in enhancing B_s, likely due to favorable microstructural changes that promote magnetization. These results confirm the effectiveness of compositional tuning in improving the soft magnetic performance of Fe-P-C alloys. Figure 4(c) presents the H_c values for different alloy compositions, showing a gradual increase with increasing Fe content, reaching 26.2 $A \cdot m^{-1}$ for $Fe_{85}P_9C_6$. Although this H_c is slightly higher than that of conventional nanocrystalline alloys such as Finemet and Nanoprm[1, 2], it remains within a practical range. Given its significantly higher B_s, $Fe_{85}P_9C_6$ offers a favorable trade-off for applications where saturation magnetization is a critical parameter. Table 1 provides a comprehensive summary of the B_s and H_c values for all alloy compositions. Figure 4(d) compares the B_s of the $Fe_{85}P_9C_6$ alloy with those of commercial AN soft magnetic materials. The results indicate that $Fe_{85}P_9C_6$ exhibits a higher B_s than several widely used commercial counterparts[22-26]. Although

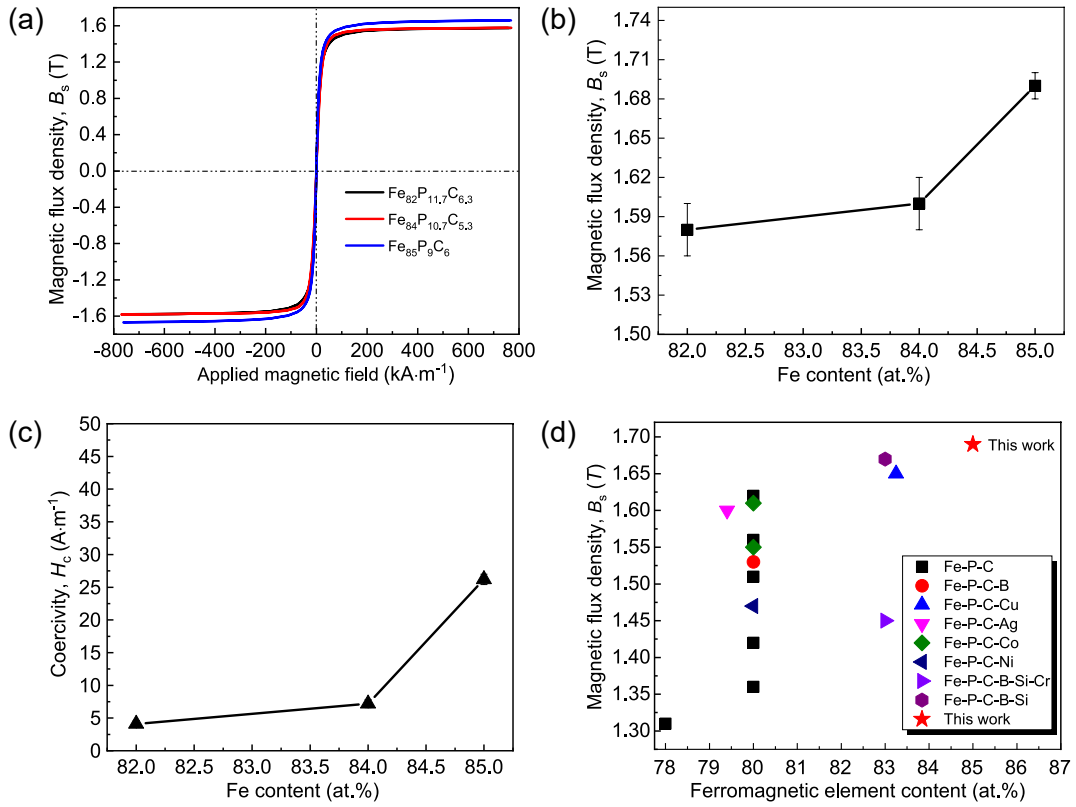

Fig. 4: *B-H* hysteresis loop curves (a), dependence of B_s and H_c on Fe content for melt-spun Fe-P-C alloy ribbons (b, c), and comparison of B_s vs. Fe content for $Fe_{85}P_9C_6$ (indicated by a star) and previously reported Fe-P-C-type alloys (d)[11, 12, 21, 28-31]

certain post-annealed nanocrystalline alloys present slightly higher B_s values[27, 28], $Fe_{85}P_9C_6$ achieves comparable magnetic performance without the need for annealing. This not only streamlines processing but also enhances mechanical ductility and reduces production costs, rendering $Fe_{85}P_9C_6$ a promising candidate for next-generation soft magnetic components, including transformers and power inductors[29, 30]. The high B_s value (1.69 T) of $Fe_{85}P_9C_6$ can be attributed to the synergistic effects of several factors: (1) Minimal intermetallic content, which reduces the influence of nonmagnetic elements and preserves high magnetic saturation[31, 32]; (2) Optimized elemental ratio, where the balanced composition of ferromagnetic Fe and nonmetallic P/C reduces *p-d* hybridization, increasing 3*d* electron holes and enhancing magnetic moments[7]; (3) Controlled cooling rate, which facilitates the formation of a fine nanocrystalline structure embedded in an amorphous matrix, contributing to improved B_s.

TEM was employed to conduct a detailed analysis of the microstructure of the $Fe_{85}P_9C_6$ as-spun alloy ribbon, with the aim of further investigating the underlying factors influencing its performance. The TEM observation data presented in Fig. 5 align with the XRD pattern analysis results shown in Fig. 1(a). In low-magnification TEM imaging, the as-spun $Fe_{85}P_9C_6$ alloy ribbon sample does not exhibit any significant contrast variations, as shown in Fig. 5(a). This uniform appearance suggests that the material possesses a relatively homogeneous structure at this magnification level. However, a closer examination through high-resolution transmission electron microscopy, depicted in Fig. 5(b), reveals a more complex structural composition. The HRTEM image demonstrates that the as-spun $Fe_{85}P_9C_6$ alloy ribbon is not entirely amorphous; rather, it exhibits a heterogeneous amorphous nature. This is characterized by the presence of regions with distinct crystal lattice fringe contrast, indicating the existence of crystalline clusters, which coexist with areas displaying irregular modulation contrast typical of the amorphous phase. The fine fringe contrast in the HRTEM image indicates that the nanocrystals are well-ordered and free from significant internal defects, such as dislocations or stacking faults, which may contribute to their favorable magnetic properties. Statistical analysis of the grain sizes in the image reveals that the clusters are approximately 5 nm in size and are randomly distributed within the amorphous matrix. The fast Fourier transform (FFT) pattern from Region A in Fig. 5(c) further confirms that these clusters have a fcc structure, indicating the formation of a highly ordered crystal structure during the cooling process. Additionally, the FFT pattern from Region B also verifies the fcc structure of the precipitated grains [Figs. 5(d) and (e)], demonstrating the consistency of the crystal structure in the local regions of the material. In soft magnetic materials, precisely controlling the nanocrystal size has a significant impact on magnetic performance. Grain sizes that are too large or too small can hinder the movement of magnetic domain walls, thereby affecting the saturation magnetic induction[17, 18].

To gain deeper insight into the evolution of magnetic domain structures under weak magnetic fields and their

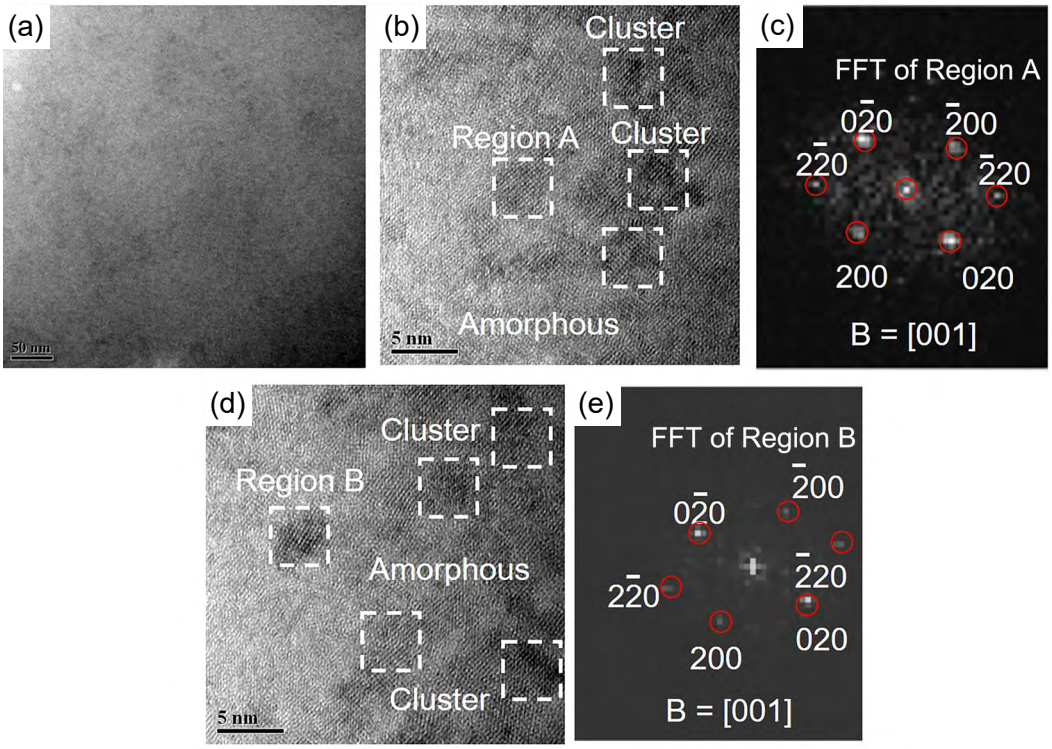

Fig. 5: TEM bright-field image (a), high-resolution TEM image (b), Fourier-transform image of Region A (c), high-resolution TEM image (d), and Fourier-transform image of Region B (e) for the melt-spun $Fe_{85}P_9C_6$ alloy ribbon sample

intrinsic relationship with soft magnetic properties, this study systematically investigates the domain evolution of the three melt-spun alloy ribbons: $Fe_{82}P_{11.7}C_{6.3}$, $Fe_{84}P_{10.7}C_{5.3}$, and $Fe_{85}P_9C_6$, during representative magnetization stages within the range of 0–1 kA·m^{-1}. The aim is to elucidate, at the domain level, how different microstructures (fully amorphous and amorphous-nanocrystalline composite states) influence the magnetization behavior. Both $Fe_{82}P_{11.7}C_{6.3}$ and $Fe_{84}P_{10.7}C_{5.3}$ exhibit typical amorphous structures and display similar magnetic domain morphologies, characterized predominantly by disordered, fingerprint-like patterns (Figs. 6 and 7). Although these materials have relatively low coercivity (H_c<10 A·m^{-1}), their domain structures lack well-defined order. This is mainly attributed to complex residual stress fields introduced during the melt-spinning process. According to the literature, the surfaces of melt-spun ribbons are generally under compressive stress, while the interior regions tend to experience tensile stress[33-35]. Such non-uniform stress distributions significantly hinder the free motion of domain walls, resulting in strong pinning effects. As the applied magnetic field increases from 0.1 to 1.0 kA·m^{-1}, the magnetization process proceeds slowly: reverse domains gradually shrink, while domains aligned with the field progressively expand, and the overall system trends toward a single magnetization direction approaching saturation. However, due to the inherent atomic disorder and the combined effects of high residual stress in the amorphous structure, the magnetic anisotropy energy is highly non-uniform in space. As a result, domain wall motion remains constrained even under a 1.0 kA·m^{-1} field, and residual fingerprint-like disordered domains are still observed [Figs. 6(f) and 7(f)].

In contrast, the $Fe_{85}P_9C_6$ sample exhibits a composite structure in which a small amount of nanocrystalline clusters precipitate within an amorphous matrix. Its domain morphology is markedly different from the other two samples, presenting narrower, more regularly aligned stripe-like domains (Fig. 8), indicating stronger in-plane magnetic anisotropy and greater domain ordering. Under low applied fields, this material exhibits a more rapid magnetization response: magnetic domains realign quickly along the direction of the external field, and reverse domains are significantly reduced [Figs. 8(a–c)]. This behavior can be attributed to the presence of nanocrystals, which not only alleviate the spatial fluctuation of residual stresses but also provide a more uniform and stable magnetic anisotropy energy distribution, thereby facilitating the cooperative motion and rapid transformation of domain walls. Benefiting from these structural advantages, the $Fe_{85}P_9C_6$ sample exhibits a higher saturation magnetic induction (B_s=1.69 T) and a relatively higher coercivity (H_c= 26.2 A·m^{-1}).

4 Discussion

Among the melt-spun $Fe_{82}P_{11.7}C_{6.3}$, $Fe_{84}P_{10.7}C_{5.3}$, and $Fe_{85}P_9C_6$ alloy ribbons, the $Fe_{85}P_9C_6$ composition exhibits a unique structure comprising an amorphous matrix embedded with nanocrystalline clusters, along with the highest B_s and excellent bending ductility. Given these advantages, detailed investigations were conducted to elucidate the phase evolution of this alloy. To probe the crystallization behavior near the exothermic peak, $Fe_{85}P_9C_6$ samples were isothermally held at temperatures ranging from 517 to 740 K, and the

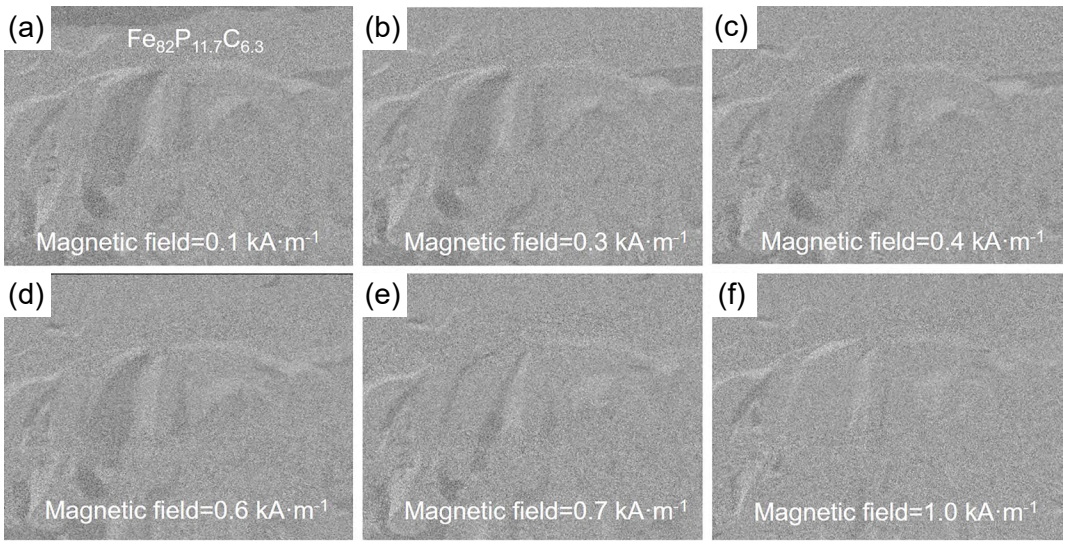

Fig. 6: Magnetic domain evolution of $Fe_{82}P_{11.7}C_{6.3}$ melt-spun ribbons under an external magnetic field ranging from 0.1 to 1.0 kA·m^{-1} (a–f)

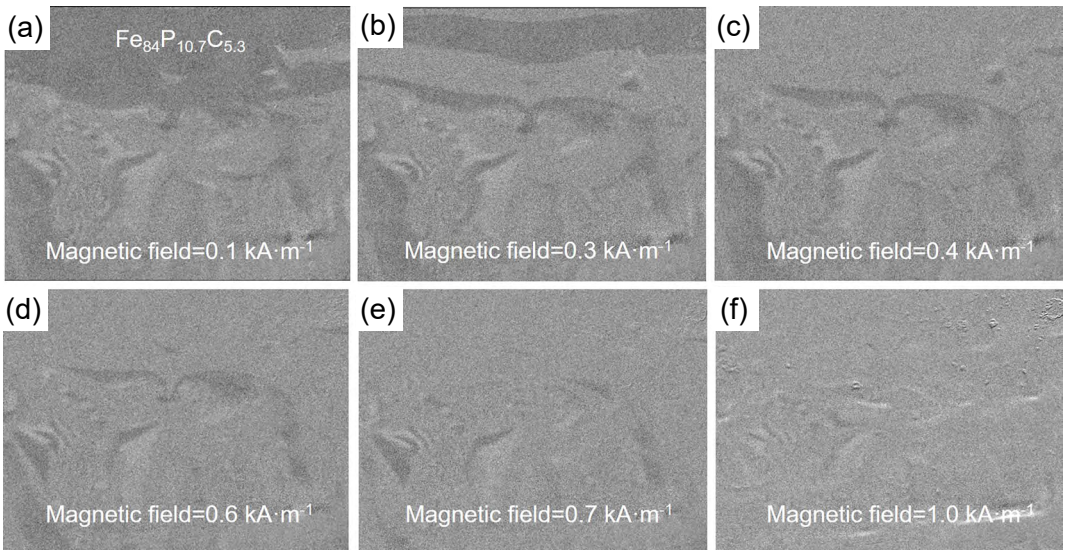

Fig. 7: Magnetic domain evolution of $Fe_{84}P_{10.7}C_{5.3}$ melt-spun ribbons under an external magnetic field ranging from 0.1 to 1.0 kA·m^{-1} (a–f)

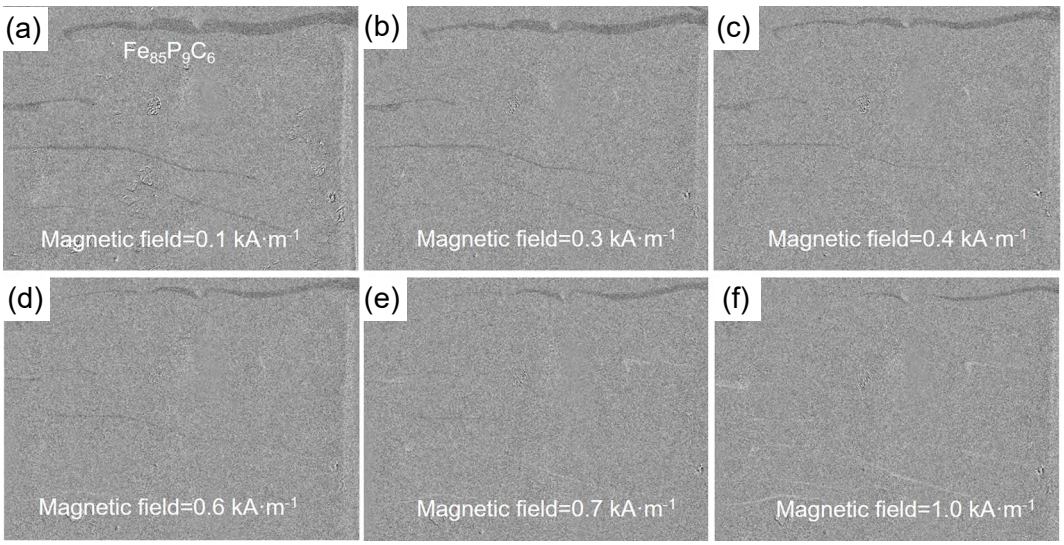

Fig. 8: Magnetic domain evolution of $Fe_{85}P_9C_6$ melt-spun ribbons under an external magnetic field ranging from 0.1 to 1.0 kA·m^{-1} (a–f)

resulting phases were identified via XRD [Fig. 9(a)]. Based on the results in Figs. 1(e) and 9(a), the first exothermic peak corresponds to the transformation from an amorphous phase with metastable fcc-(Fe, P, C) clusters to a mixture of residual amorphous matrix and α-Fe, while the second peak is associated with the formation of α-Fe, Fe_3C, and Fe_3P. Accordingly, the overall crystallization sequence can be described as: [amorphous+fcc-(Fe, P, C)] → [amorphous′ + α-Fe] → [α-Fe+Fe_3C+Fe_3P]. To facilitate better control over structural evolution and property optimization during thermal processing, the crystallization behavior of the melt-spun $Fe_{85}P_9C_6$ alloy was further analyzed through continuous-cooling-transformation (CCT) and continuous-heating-transformation (CHT) diagrams, as illustrated in Fig. 9(b). Curve A denotes the cooling path during solidification, while Curves B and C represent typical heating paths during annealing. The diagrams reveal that a well-controlled cooling rate not only stabilizes the amorphous matrix but also enables the formation of nanocrystals with an fcc structure. This confirms the feasibility of engineering dual-phase microstructures consisted of amorphous and nanocrystalline through appropriate thermal strategies. Furthermore, these transformation diagrams offer insights into the nucleation and growth mechanisms governing structural transitions, thereby providing a basis for tailoring the magnetic and mechanical properties of the material.

Figure 9(a) shows that the fcc-(Fe, P, C) phase is metastable, gradually diminishing with increased annealing temperature or prolonged holding time. The Goldschmidt atomic radii of Fe, P, and C are 1.28 Å, 1.09 Å, and 0.77 Å, respectively[36], leading to considerable atomic size mismatch and consequently high internal lattice stress within the fcc-(Fe, P, C) phase. Such lattice distortions elevate the system's free energy, rendering the phase thermodynamically unstable. Upon heating, this phase tends to transform into the more stable α-Fe phase, a transition driven by energy minimization. This transformation behavior is thus closely related to the elemental size disparity and the associated internal strain. Similar transitions have been reported in other alloy systems. For example, in Fe-P-C-B nanocrystalline alloys, a metastable fcc-(Au, P) phase was observed to transform into α-Fe during annealing[37]. This transformation typically initiates at heterogeneous nucleation sites provided by the residual fcc phase, further supporting the thermodynamic instability of the fcc-type structures and their role as precursors for α-Fe crystallization.

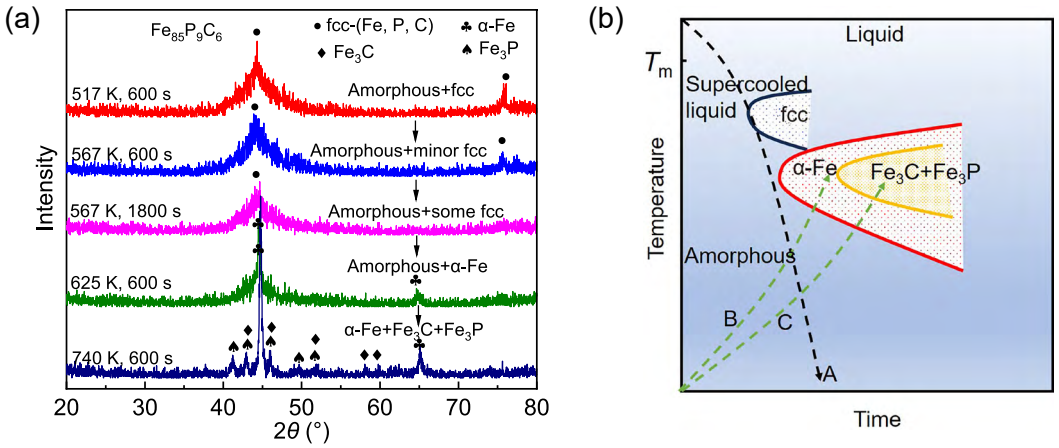

Fig. 9: XRD patterns of $Fe_{85}P_9C_6$ melt-spun alloy ribbons annealed at various temperatures and times (a) and CCT and CHT curves for alloy (b)

5 Conclusions

By rationally optimizing the composition of conventional nanocrystalline alloys, costly elements such as Cu, Ag, and Nb were effectively eliminated. A simplified Fe-P-C system was established, characterized by increased Fe content and reduced P content, which facilitates the formation of quenched clusters, improves magnetic properties, and enhances bending ductility. This compositional design enable the direct formation of a novel microstructure composed of amorphous and cluster in the as-quenched $Fe_{85}P_9C_6$ alloy. The resulting material exhibits thermal stability up to 569 K, high Vickers hardness of 621 HV, and excellent mechanical ductility. Upon annealing, the crystallization process proceeds via the transformation of a metastable fcc-(Fe, P, C) phase into α-Fe, Fe_3C, and Fe_3P, a transition driven by internal stresses arising from atomic size mismatch.

Magnetic domain structure analysis under low magnetic fields (0–1 kA·m^{-1}) further highlights the microstructural influence on magnetic behavior. The fully amorphous alloys $Fe_{82}P_{11.7}C_{6.3}$ and $Fe_{84}P_{10.7}C_{5.3}$ exhibit disordered, fingerprint-like domains and sluggish magnetization dynamics, primarily attributed to stress-induced fluctuations in magnetic anisotropy, with corresponding B_s values ranging from 1.58 to 1.60 T and H_c between 4.1 and 7.2 A·m^{-1}. In contrast, the $Fe_{85}P_9C_6$ alloy, with its dual-phase amorphous-nanocrystalline structure, displays well-aligned stripe domains, accelerated domain wall motion, and enhanced anisotropy, yielding B_s=1.69 T and H_c= 26.2 A·m^{-1}.

In summary, this study establishes a clear correlation

between microstructural features and magnetic performance in Fe-rich alloys, and proposes a cost-effective, annealing-free strategy for the development of high-performance soft magnetic materials. These findings provide a valuable foundation for the design and processing of next-generation nanocrystalline magnetic alloys.

Acknowledgments

The authors would like to express their gratitude for the support received from the National Natural Science Foundation of China (No. 52202213), the Shandong Province Youth Fund (Nos. ZR2024QE439, ZR2024QE532), the Scientific Research Fund of Dezhou University (No. 30103540), the China Postdoctoral Science Foundation (No. 2023M730905), and the Science Research Project of the Hebei Education Department (No. QN2024031).

Conflict of interest

The authors declare that they have no known competing financial interests or personal relationships that could have appeared to influence the work reported in this paper.

References

[1] Yoshizawa Y, Oguma S, Yamauchi K. New Fe-based soft magnetic alloys composed of ultrafine grain structure. J. Appl. Phys., 1998, 64: 6044–6046. https://doi.org/10.1063/1.342149.

[2] Suzuki K, Makino A, Inoue A, et al. Soft magnetic properties of nanocrystalline bcc Fe-Zr-B and Fe-M-B-Cu (M = transition metal) alloys with high saturation magnetization. J. Appl. Phys., 1991, 70: 6232–6237. https://doi.org/10.1063/1.350006.

[3] Willard M A, Laughlin D E, McHenry M E, et al. Structure and magnetic properties of $(Fe_{0.5}Co_{0.5})_{88}Zr_7B_4Cu_1$ nanocrystalline alloys. J. Appl. Phys., 1998, 84: 6773–6777. https://doi.org/10.1063/1.369007.

[4] Makino A, Inoue A, Masumoto T. Nanocrystalline soft magnetic Fe-M-B (M=Zr, Hf, Nb) alloys produced by crystallization of amorphous phase. Mater. Trans., 1995, 36: 924–938. https://doi.org/10.2320/matertrans1989.36.924.

[5] Chen F G, Wang Y G, Miao X F, et al. Nanocrystalline $Fe_{83}P_{16}Cu_1$ soft magnetic alloy produced by crystallization of its amorphous precursor. J. Alloys Compd., 2013, 549: 26–29. https://doi.org/10.1016/j.jallcom.2012.09.072.

[6] Skorvánek I, Duhaj P, Kovác J, et al. Influence of microstructure on magnetic and mechanical behavior in amorphous and nanocrystalline $Fe_{73.5}Nb_{4.5}Cr_5Cu_1B_{16}$ alloy. Mater. Sci. Eng. A, 1997, 226–228: 218–222.

[7] Li X S, Zhou J, Shen L Q, et al. Exceptionally high saturation magnetic flux density and ultralow coercivity via an amorphous-nanocrystalline transitional microstructure in an FeCo-based alloy. Adv. Mater., 2022, 35: 2205863.

[8] Xu J, Yang Y Z, Li W, et al. Effect of P addition on glass forming ability and soft magnetic properties of melt-spun FeSiBCuC alloy ribbons. J. Magn. Magn. Mater., 2016, 417: 291–293. https://doi.org/10.1016/j.jmmm.2016.05.103.

[9] Hou L, Shen P F, Wang B J, et al. Dynamic relaxation behavior and its effect on mechanical properties of FePBCCu amorphous alloy. Mater. Today Commun., 2023, 35: 106012. https://doi.org/10.1016/j.mtcomm.2023.106012.

[10] Duwez P, Lin S C H. Amorphous ferromagnetic phase in iron-carbon-phosphorus alloys. J. Appl. Phys., 1967, 38: 4096–4097. https://doi.org/10.1063/1.1709084.

[11] Wang J F, Li R, Hua N B, et al. Ternary Fe-P-C bulk metallic glass with good soft-magnetic and mechanical properties. Scripta Mater., 2011, 65: 536–539. https://doi.org/10.1016/j.scriptamat.2011.06.020.

[12] Li Q, Li J, Gong P, et al. Formation of bulk magnetic ternary Fe80P13C7 glassy alloy. Intermetallics, 2012, 26: 62–65. https://doi.org/10.1016/j.intermet.2012.03.045.

[13] Murugaiyan P, Bedanta S, Jena S K, et al. Crystallization and magnetic hardening behaviour of Fe-rich FeSiBNb(Cu) melt-spun alloys. J. Magn. Magn. Mater., 2020, 502: 166528. https://doi.org/10.1016/j.jmmm.2020.166528.

[14] Jafari S, Beitollahi A, Yekta B E, et al. Atom probe analysis and magnetic properties of nanocrystalline Fe84.3Si4B8P3Cu0.7. J. Alloys Compd., 2016, 674: 136–144. https://doi.org/10.1016/j.jallcom.2016.03.005.

[15] Zuo M Q, Meng S Y, Li Q, et al. Effect of metalloid elements on magnetic properties of Fe-based bulk metallic glasses. Intermetallics, 2017, 83: 83–86. https://doi.org/10.1016/j.intermet.2016.12.010.

[16] Takeuchi A, Inoue A. Classification of bulk metallic glasses by atomic size difference, heat of mixing and period of constituent elements and its application to characterization of the main alloying element. Mater. Trans., 2005, 12: 2817–2829. https://doi.org/10.2320/matertrans.46.2817.

[17] Pang L L, Inoue A, Zanaeva E N, et al. Nanocrystalline, good soft magnetic properties and ultrahigh mechanical strength for $Fe_{82\text{-}85}B_{13\text{-}16}Si_1Cu_1$ amorphous alloys. J. Alloys Compd., 2019, 785: 25–37. https://doi.org/10.1016/j.jallcom.2019.01.150.

[18] Liu C, Inoue A, Kong F L, et al. Fe-B-Si-C-Cu amorphous and nanocrystalline alloys with ultrahigh hardness and enhanced soft magnetic properties. J. Non-Cryst. Solids., 2021, 554: 120606. https://doi.org/10.1016/j.jnoncrysol.2020.120606.

[19] Dong C, Inoue A, Wang X H, et al. Soft magnetic properties of $Fe_{82\text{-}83}B_{14\text{-}15}Si_2C_{0.5\text{-}1}$ amorphous alloys with high saturation magnetization above 1.7 T. J. Non-Cryst. Solids, 2018, 500: 173–180. https://doi.org/10.1016/j.jnoncrysol.2018.07.072.

[20] Kim Y, Hwang B. Effects of metalloid elements on the mechanical properties of Fe-based bulk amorphous alloys. Korean J. Mater. Res., 2016, 26: 671–675. http://dx.doi.org/10.3740/MRSK.2016.26.12.671.

[21] Zhou S X, Dong B S, Qin J Y, et al. The relationship between the stability of glass-forming Fe-based liquid alloys and the metalloid-centered clusters. J. Appl. Phys., 2012, 112: 023514.

[22] Han Y, Kong F L, Han F F, et al. New Fe-based soft magnetic amorphous alloys with high saturation magnetization and good corrosion resistance for dust core application. Intermetallics, 2016, 76: 18–25. https://doi.org/10.1016/j.intermet.2016.05.011.

[23] Suzuki K, Parsons R, Zang B, et al. Copper-free nanocrystalline soft magnetic materials with high saturation magnetization comparable to that of Si steel. Appl. Phys. Lett., 2017, 110: 012407. https://doi.org/10.1063/1.4973772.

[24] Molotilov B V, Sadchikov V V. Amorphous soft magnetic materials and their application. J. Magn. Magn. Mater., 1992, 112: 253–257. https://doi.org/10.1016/0304-8853(92)91167-R.

[25] Madugundo R, Geoffroy O, Waeckerle T, et al. Improved soft magnetic properties in nanocrystalline FeCuNbSiB Nanophy® cores by intense magnetic field annealing. J. Magn. Magn. Mater., 2017, 422: 475–478. https://doi.org/10.1016/j.jmmm.2016.09.063.

[26] Ohta M, Yoshizawa Y. Magnetic properties of nanocrystalline $Fe_{82.65}Cu_{1.35}Si_xB_{16\text{-}x}$ alloys (x=0–7). Appl. Phys. Lett., 2007, 91: 062517. https://doi.org/10.1063/1.2769956.

[27] Urata A, Yamaki M, Takahashi M, et al. Low core loss of non-Si quaternary $Fe_{83.3}B_8P_8Cu_{0.7}$ nanocrystalline alloy with high B_s of 1.7 T. J. Appl. Phys., 2012, 111: 07A345–07A335. https://doi.org/10.1063/1.3679467.
[28] Wang A D, Men H, Shen B L, et al. Effect of P on crystallization behavior and soft-magnetic properties of $Fe_{83.3}Si_4Cu_{0.7}B_{12-x}P_x$ nanocrystalline soft-magnetic alloys. Thin Solid Films, 2011, 519: 8283–8286. https://doi.org/10.1016/j.tsf.2011.03.110.
[29] Wang J F, Di Y X, Fang Z, et al. Thermal stability, crystallization and soft magnetic properties of Fe-P-C-based glassy alloys. J. Non-Cryst. Solids, 2016, 454: 39–45. https://doi.org/10.1016/j.jnoncrysol.2016.10.014.
[30] Li W, Yang Y H, Xie C X, et al. Glass formation, crystallization and magnetic properties of high-Fe Fe-metalloid (B, C, and P) melt-spun ribbons. J. Magn. Magn. Mater., 2019, 498: 166128. https://doi.org/10.1016/j.jmmm.2019.166128.
[31] Gao J G, Du Q, Ren H T, et al. Effect of Ag microalloying on the magnetic properties and microstructure of Fe-P-C amorphous alloys. J. Alloys Compd., 2023, 960: 171067. https://doi.org/10.1016/j.jallcom.2023.171067.
[32] Jin Y L, Fan X D, Men H, et al. FePCCu nanocrystalline alloys with excellent soft magnetic properties. Sci. China, 2012, 55: 3419–3424. https://doi.org/10.1007/s11431-012-4928-0.
[33] Hou L, Shang Q Z, Yang H, et al. Effects of oxygen on thermal behavior and magnetic properties of FePC amorphous alloy. J. Non-Cryst. Solids, 2022, 581: 121413. https://doi.org/10.1016/j.jnoncrysol.2022.121413.
[34] Hou L, Li M R, Jiang C, et al. Thermal and magnetic properties of Fe(Co)BCCu amorphous alloys with high saturation magnetization of 1.77 T. J. Alloys Compd., 2021, 853: 157071. https://doi.org/10.1016/j.jallcom.2020.157071.
[35] Zhao C L, Wang A D, He A N, et al. Correlation between soft-magnetic properties and T_{x1}–T_c in the high B_s FeCoSiBPC amorphous alloys. J. Alloys Compd., 2016, 659: 193–197. http://dx.doi.org/10.1016/j.jallcom.2015.11.044.
[36] Wang H, Hu T, Zhang T. Atomic, electronic and magnetic properties of $Fe_{80}P_{11}C_9$ amorphous alloy: A first-principles study. Physica B, 2013, 411: 161–165. https://doi.org/10.1016/j.physb.2012.11.044.
[37] Han M H, Sun C, Xi G G, et al. Decomposition of pre-existing Au-P clusters induced in situ α-Fe grains uniformization in Fe-P-based nanocrystalline alloys. Rare Met., 2024, 43: 5242–5255. https://doi.org/10.1007/s12598-024-02707-8.